Available online at www.sciencedirect.com

SciVerse ScienceDirect

Acta Materialia 60 (2012) 4646–4660

Acta MATERIALIA

www.elsevier.com/locate/actamat

A macro- and micromechanics investigation of hot cracking in duplex steels

Guilhem Martin [a,*], Sampath Kumar Yerra [b], Yves Bréchet [a], Muriel Véron [a], Jean-Denis Mithieux [c], Béchir Chéhab [c], Laurent Delannay [b], Thomas Pardoen [b]

[a] *Laboratoire de Science et Ingéniérie des Matériaux et Procédés, Groupe Physique du Métal, Domaine Universitaire, 1130 Rue de la Piscine, 38402 Saint Martin d'Hères, France*

[b] *Institute of Mechanics, Materials and Civil Engineering, Université Catholique de Louvain, Place Sainte Barbe 2, B-1348 Louvain-la-Neuve, Belgium*

[c] *Aperam Research Center, BP 15, 62230 Isbergues, France*

Received 19 December 2011; accepted 21 March 2012
Available online 3 May 2012

Abstract

The relationship between microstructure and high temperature ductile tearing in duplex stainless steels has been investigated. Several grades were considered corresponding to different chemical compositions, different volume fractions and morphologies of the ferrite and austenite phases and different oxide inclusion contents. The high temperature cracking resistance has been quantified using both the essential work of fracture (EWF) and the fracture strain. The EWF discriminates the different grades of duplex steels and the different microstructures in terms of hot tearing resistance better than does the fracture strain. Metallographic characterization reveals that damage preferentially nucleates near inclusions at the austenite/ferrite boundary. Voids grow inside the ferrite until they coalesce. Damage develops more rapidly when increasing either the mismatch of rheology between the phases, which was evaluated by micro-scale strain measurements, or the inclusion content. The cracking resistance is related to the plastic work performed in the fracture process zone whereas the fracture strain depends on the damage kinetics. Both processes involve length scales related to the morphology and to the microstructure dimensions. Guidelines for improving the hot cracking resistance of duplex steels are formulated.

Keywords: Duplex stainless steels; Crack propagation; Micromechanics; High temperature deformation; Essential work of fracture

1. Introduction

Duplex stainless steels (DSSs) consist of a two phase microstructure involving δ-ferrite and γ-austenite. An exceptional combination of strength and toughness together with good corrosion resistance under critical working conditions designate DSS as suitable alternatives to conventional austenitic stainless steels. This good structural performance explains their use in a variety of applications, particularly in the petroleum and gas industries, as well as in chemical vessel applications [1].

Unfortunately, the poor hot workability of these alloys makes the industrial processing of flat products particularly critical. Cracking along the edges of the coils during hot rolling is frequently reported [2,3]. As a consequence, additional operations like grinding, discontinuous processing or scraping are often required, increasing the manufacturing costs. The high temperature mechanical behaviour of DSS depends on several phenomena: phase proportions [4], chemical composition [2], impurities [2,5], size and morphology of both phases [6,7], nature of the interphase boundaries [8], softening mechanisms in the constituting phases [9–13], and strain partitioning between ferrite and austenite [3,14]. A fundamental research effort is thus needed in order to unravel the mechanisms at the origin of a reduction in toughness at high temperature. Only the

* Corresponding author. Tel.: +33 (0) 476826707; fax: +33 (0) 476826644.
E-mail addresses: guilhem.martin@simap.grenoble-inp.fr, gui12@hotmail.fr (G. Martin).

1359-6454/$36.00 © 2012 Acta Materialia Inc. Published by Elsevier Ltd. All rights reserved.
http://dx.doi.org/10.1016/j.actamat.2012.03.040

use of a multiscale approach can link the cracking resistance to the relevant microstructural characteristics.

One of the main difficulties in hot cracking studies is the definition of a relevant material parameter characterizing the fracture resistance and capturing its sensitivity to the controlling phenomena. In some applications the resistance to damage initiation and growth is the main issue. In such cases the high temperature fracture strain measured on tensile specimens usually provides valuable information. In other applications the resistance to cracking initiation from stress concentration is the main issue. Finally, the tearing resistance, i.e. the resistance to the propagation of a crack, is the key parameter for edge cracking during hot rolling. At high temperatures the classical approach to non-linear fracture mechanics is most of the time not valid, due to extreme ductility and rate sensitivity, especially if the initial cracks are short [15].

Recently, the essential work of fracture method has been successfully applied to characterize the high temperature tearing resistance of ferritic stainless steel [16]. The EWF concept has been widely used over the last 35 years to quantify the fracture resistance of ductile metallic materials sheets (brass, bronze, zinc alloys, aluminium alloys and steels) [17–22] or polymer thin sheets or layers [23–26]. The EWF represents the work per unit area spent in the fracture process zone. It is computed over the complete duration of ligament cracking (see Fig. 1). This work represents the energy spent locally at the crack tip due to damage and necking. Using micromechanics arguments it can be related to the physical mechanisms of failure and to the microstructure. This is essential in the context of the present study. The major advantages of the EWF method are that it does not require any monitoring of crack propagation and that it can be used in circumstances where non-linear fracture mechanics concepts, such as the J integral, cannot be applied. Nevertheless, application of the EWF method at temperatures above ambient is not common. It has been used at intermediate temperatures (100–300 °C) on polymers [27,28] inside a furnace. Applying the EWF concept is an experimental challenge for higher temperatures (>1000 °C). In addition to the difficulties of controlling the microstructures at high temperature in materials affected by phase transformations, carrying out the test in a homogeneous temperature furnace requires special care [16].

The objective of the present work is to address the high temperature fracture resistance of DSSs using the EWF concept. Using further characterizations and models we aim to establish the link between such fracture energy, the microstructure and the failure mechanisms in order to guide materials optimization. The EWF is expected to be sensitive to the alloy composition and to the microstructural parameters, such as the γ phase morphology or the inclusion content. As a preliminary task, model microstructures with different γ morphologies (equiaxed (E) or Widmanstätten (W)) were generated while controlling the phase proportion and the size of the γ phase. For that purpose, three different duplex steels were investigated, D1, D1bis and D2, with different inclusion contents. The materials in the as-cast conditions were also tested for comparison. Different parameters characterizing the high temperature fracture resistance have been measured and assessed: (i) the equivalent fracture strain ($\varepsilon^{eq}_{fracture}$); (ii) a mean damage nucleation strain ($\varepsilon^{eq}_{damage}$); and (iii) the tearing resistance determined by the EWF (w_e). These tests have been supplemented by in-depth analysis of the microstructure and damage mechanisms.

The outline of the paper is as follows. The materials and the experimental procedures are described in Section 2. Section 3 presents the experimental results, which are discussed in depth in Section 4. The discussion addresses the influence of the microstructural parameters on the high

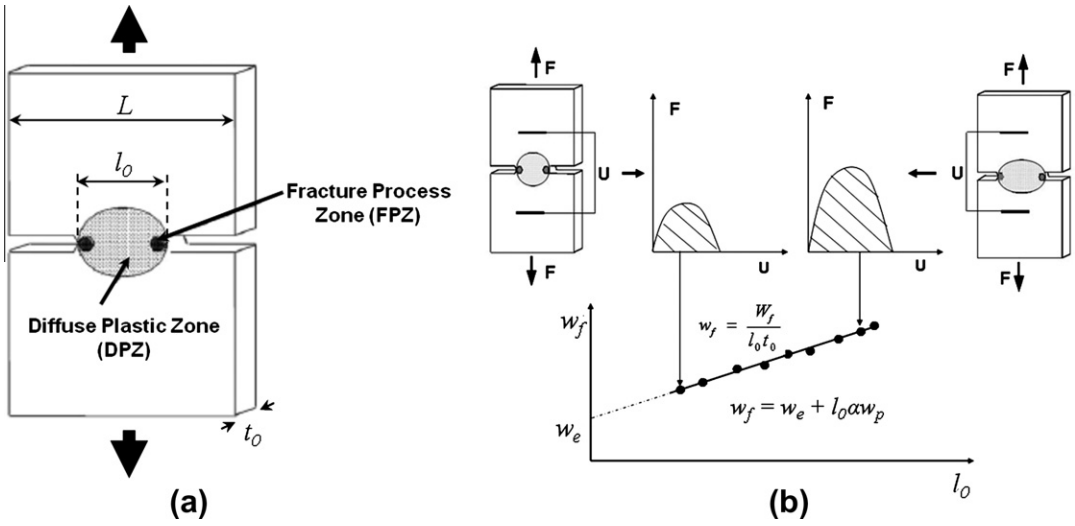

Fig. 1. (a) DENT geometry showing the diffuse plastic zone as well as the localized necking zone in front of the crack tips. (b) Diagram illustrating the method to determine the specific essential work of fracture.

temperature fracture resistance of duplex steels: (i) the influence of microstructural heterogeneities; (ii) the influence of the phase rheology; (iii) the influence of the inclusion content; (vi) the influence of the phase morphology. A summary of the main results finally leads to recommendations regarding the enhancement of DSS high temperature fracture resistance.

2. Materials and experimental procedures

2.1. Materials

The chemical compositions of the three grades D1, D1bis and D2 are given in Table 1. Grades D1 and D1bis correspond to a commercial alloy 2205 DSS (alloy 1.4462 according to EN 10088) but belong to different industrial castings involving slight differences in chemical composition. Grade D2 is an industrial test material known to have poor hot rolling properties with systematic occurrence of 50 mm edge crack lengths. In contrast, cracks in D1, when they are present, do not exceed 5 mm in length.

The microstructures of grades D1 and D2 in the as-cast conditions are shown in Fig. 2a and b, respectively. The schematic equilibrium phase diagram provides indications about the microstructure evolution during processing (Fig. 3). From liquid the alloy solidifies as δ-ferrite (Fig. 3a). During cooling the γ phase precipitates by a mechanism of nucleation and growth. Allotriomorphic γ nucleates at existing δ grain boundaries (Fig. 3b). Widmanstätten γ laths nucleate from the allotriomorphic γ with a Kurdjumov–Sachs orientation relationship [29–31] (Fig. 3c) (the Kurdjumov–Sachs orientation relationship was verified by EBSD analysis).

Starting from the same metallurgical hot rolled conditions, microstructures of either Widmanstätten laths (W) or equiaxed γ-austenite (E) were developed with the same amount of γ phase, stable at 1050 °C, which is the fracture test temperature. After heat treatment the specimens were polished down to 1 μm and etched with a 40% aqueous NaOH electrolytic solution under a tension of 3 V. Volume fractions of each phase, γ lath thickness and grain size distributions were determined by image analysis using Aphelion™ software [32]. A proper understanding of the as-cast microstructures permits the definition of an appropriate heat treatment to generate a Widmanstätten morphology (see Fig. 4a). The resulting microstructures corresponding to each duplex grade, D1_W, D1bis_W and D2_W, are also shown in Fig. 4a. The heat treatments required to produce

Table 1
Chemical composition (wt.%) of the grades investigated.

	Cr	Ni	Mo	Mn	Si	Cu	C	N
D1	22.90	5.59	3.11	1.75	0.55	0.19	0.02	0.17
D1bis	22.67	5.57	3.21	1.76	0.68	0.20	0.02	0.17
D2	21.96	2.99	0.91	2.88	0.39	0.67	0.03	0.18

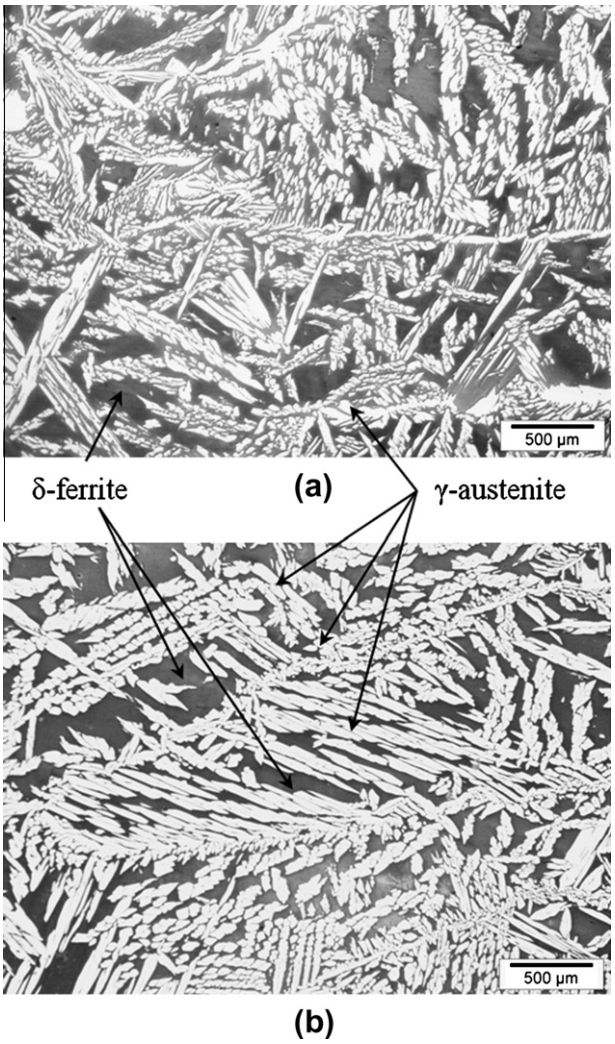

Fig. 2. Microstructures in the as-cast conditions: (a) D1; (b) D2.

an equiaxed γ morphology and the resulting microstructures D1bis_E and D2_E are shown in Fig. 4b. The proportion of γ phase, the mean thickness of the γ laths (e_γ) in the Widmanstätten morphology and the average size of the γ islands (d_γ) in the equiaxed morphology are given in Table 2. These values were obtained by averaging a set of 20 micrographs for each microstructure. The error is then evaluated by computing the standard deviation.

2.2. Experimental procedures

2.2.1. High temperature fracture tests

The EWF concept was introduced by Cotterell and Reddel [33] as a way of quantifying the fracture resistance of thin ductile metallic sheets. The EWF concept tackles the complete fracture of a specimen and not only the initiation, such as in fracture mechanics. Based on dimensional considerations, the work dissipated within the plastic zone is withdrawn from the total work of fracture. This provides an estimate of the work spent per unit area within the fracture process zone (FPZ) to break the material [34,35]. If plasticity is confined to the ligament of a sheet specimen

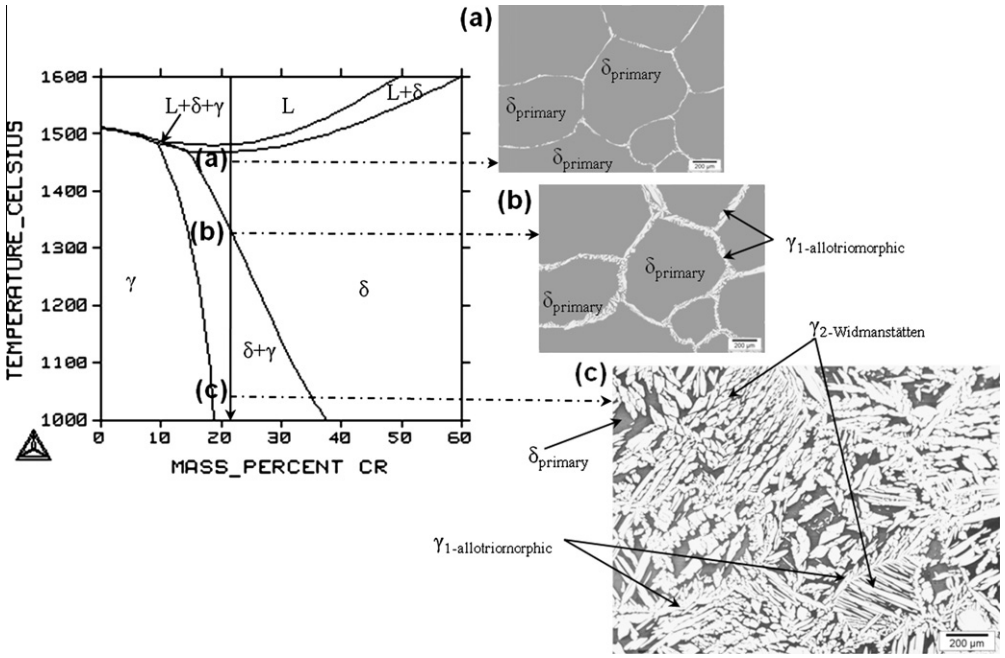

Fig. 3. Origin of the as-cast microstructure in duplex stainless steel. (a) At high temperature duplex stainless steel is entirely ferritic. During cooling, the austenite precipitates (b) at existing ferrite grain boundaries and (c) inside the ferrite matrix with a lath morphology. The thermal history explains the as-cast microstructure.

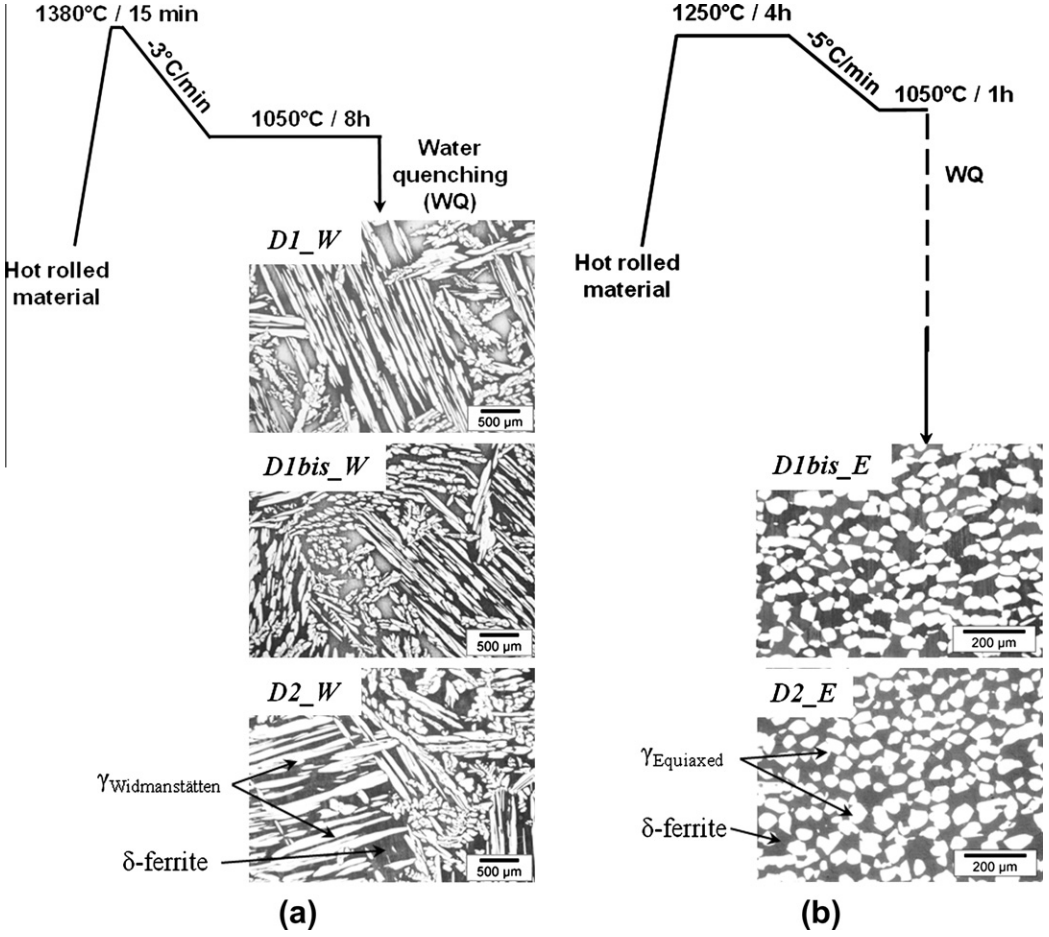

Fig. 4. (a) Schematic representation of the heat treatment to generate a Widmanstätten austenite (W) and resulting microstructures: D1_W, D1bis_W, and D2_W. (b) Schematic of the heat treatment to produce an equiaxed austenite (E) and resulting microstructures: D1bis_E and D2_E.

Table 2
Volume fraction of austenite and average thickness of the laths for the Widmanstätten microstructure or average size of the austenite islands for the equiaxed morphology.

	D1_W	D1bis_W	D2_W	D1bis_E	D2_E
γ-Austenite (%)	46 ± 3	44 ± 3	51 ± 3	47 ± 3	52 ± 3
$e_{\gamma\text{-austenite}}$ (μm)	49 ± 2	49 ± 2	61 ± 3		
$d_{\gamma\text{-austenite}}$ (μm)				50 ± 3	59 ± 2

before crack initiation, as shown in Fig. 1a, then the plastic work dissipated during fracture is proportional to the plastic volume at crack initiation, whereas the work in the FPZ is proportional to the fracture area. That is, the plastic work and the EWF scale differently with sample dimensions. The double edge notch tension (DENT) geometry is particularly well suited to thin sheets (Fig. 1a), due to the symmetry and the absence of buckling. The total plastic work dissipated during the test is proportional to the volume of the plastic zone, which can be approximated by the product of the initial thickness t_0 and of the area contained in an ellipse of which one of the axes is the initial ligament length l_0. The work performed in the FPZ is proportional to the ligament area $l_0 t_0$. The total work of fracture W_f is the sum of the essential work W_e and the plastic work W_p:

$$W_f = W_e + W_p = t_0 l_0 w_e + \alpha t_0 l_0^2 w_p \quad (1)$$

where w_e is the specific essential work of fracture (work per unit area), w_p is an average plastic work density (work per unit volume), and α is a shape factor ($\pi/4$ for a circular plastic zone). Normalizing the previous equation by the ligament area, the specific work of fracture $w_f = W_f/t_0 l_0$ is given by:

$$w_f = w_e + l_0 \alpha w_p \quad (2)$$

Since the term αw_p in Eq. (2) does not depend on the ligament length, w_f must vary linearly as a function of l_0. Hence, if several DENT specimens with different ligament lengths l_0 are tested, the specific essential work of fracture w_e is the constant term in the linear regression (Fig. 1b).

High temperature tensile tests were carried out on DENT specimens using a thermo-mechanical Gleeble-3500 simulator equipped with a direct resistance heating system. The specimens were resistance-heated. The temperature is measured by a thermocouple controlled by a computer. The thermocouple controlling the temperature was welded next to the tip of the pre-crack. Chehab et al. [16] showed that locating the thermocouple in the centre of the ligament leads to a strong temperature gradient between the middle of the ligament and the end of the notch. This strong gradient is caused by the crack current concentration effect. Controlling the temperature with a thermocouple next to the crack tip provides a homogeneous temperature throughout the ligament. However, a significant temperature gradient develops between the ligament and the head of the specimens. This gradient helps to confine plasticity in the ligament while the remainder of the sample is purely elastic. Hence, local plastic yielding is avoided at the gripping system, making the overall load–displacement results sufficiently accurate for data reduction, i.e. there is no need for a local extensometer. For measurement of the EWF, 3 mm thick DENT plates with various ligament lengths ranging from 15 to 39 mm were heated at 1050 °C, annealed for 30 s at this temperature, and deformed under uniaxial tension at 10 mm s^{-1} grip displacement rate. Heating was stopped just before starting the test in order to avoid a sudden increase in temperature during cracking. Indeed, since the current is constant, if the area of the sample cross-section decreases, the temperature increase may be dramatic, possibly producing local fusion. The pre-crack had an initial opening of ~0.5 mm, the smallest that can be obtained by machining. This initial opening is small enough compared with the critical crack tip opening displacement obtained at high temperature (~1 mm).

The total specific work of fracture w_f is calculated from the area under the load–displacement curves. Fig. 1b shows the variation in the total specific work of fracture as a function of the ligament length l_0, exhibiting the expected linear relationship. The accuracy of αw_p and w_e is quantified as plus or minus the standard deviations s_a and s_b on the slope and the constant term in the linear regression, respectively (Appendix A).

2.2.2. Fractography

The fracture surfaces were systematically observed by scanning electron microscopy (SEM) in order to characterize the failure mechanisms and to measure the thickness of the DENT specimen at fracture t_f. Neglecting the strain component in the direction of crack propagation [36] and assuming plastic incompressibility, the average equivalent fracture strain is estimated as:

$$\varepsilon_{\text{fracture}}^{\text{eq}} = (2/\sqrt{3})\ \ln(t_f/t_0) \quad (3)$$

where t_f is the thickness at fracture.

Sections cut perpendicular to the ligament were polished in order to estimate the number of voids per unit area as a function of strain. For this purpose the section was divided into different zones with a step of 500 μm. Finally, the voids were manually counted in each region. The equivalent strain in each region was estimated as:

$$\varepsilon_i^{\text{eq}} = (2/\sqrt{3}) \ln(t_i/t_0) \quad (4)$$

where t_i is the thickness of the sample at a position i from the fracture surface. The thickness t_i was measured in the middle of each region. The plane strain assumption (zero strain in the cracking direction) becomes less relevant when the distance from the crack plane increases.

2.2.3. Inclusion quantification

The inclusion content was determined using both a manual and an automatic method on DSS sections polished down to 1 μm with a diamond paste. A set of 50 SEM

micrographs was analysed. Each micrograph was obtained using back-scattered electron contrast in order to distinguish the γ and δ phases at a magnification of 500×. Back-scattered contrast allows detection of the inclusions (in black) owing to the lower atomic mass compared with the metallic matrix. Then, the number of particles per micrograph was determined by manual counting. The inclusions were classified according to their location, i.e. in the δ-ferrite, in the γ-austenite or at the δ/γ boundary. The second method relied on the software INCAFeature developed by Oxford Instruments™ [37]. The electron back-scattered contrast was used to automatically detect the particles due to a different grey level compared with the δ + γ microstructure. A magnification of 700× was selected, corresponding to a surface of 0.0215 mm^2 per field. Several hundred fields were considered to analyse 20 mm^2. The chemical composition of the particles was determined by energy dispersive spectroscopy (EDS). The results must be analysed with caution. Indeed, for particles having a diameter between 1 and 3 μm, the interaction volume being about 1 μm^3, the chemical analysis can be affected by the matrix. In addition, the EDS technique does not allow discrimination between Mo and S because the energy of the K radiation of S coincides with the energy of the L radiation of Mo. The two techniques are complementary. The manual method allows location of the particle, but over a ~2 mm^2 surface, and no information about the nature of the particles is available. With the automatic technique, the area of analysis is about 20 mm^2, and the particle composition and size distribution can be determined.

3. Experimental results

The results of the EWF extraction are given in Fig. 5 for the different tested microstructures showing the expected linear trends. The fracture surface of each microstructure is shown in Fig. 6. The damage characterization is presented in Fig. 7. Since strain corresponding to the onset of void nucleation cannot be accurately determined, the following criterion was selected. The evolution of the void density as a function of strain can be divided into two parts. During the first stage the density of voids is close to zero and does not significantly increase. During the second stage the rate of damage is much larger. The onset of void nucleation is defined as the strain corresponding to the start of the second regime, termed $\varepsilon^{eq}_{damage}$, as shown by the arrows in Fig. 7.

The inclusions were characterized qualitatively as well as quantitatively, but only for the Widmanstätten model microstructures. The chemical analysis performed by EDS on polished samples has shown that the majority of the inclusions are oxides involving undesirable chemical elements such as Al, Ca or Mg. These elements were present during elaboration of the alloy during manufacture: Al is added during processing in order to reduce oxides; Ca is used to trap sulphur and, hence, to reduce its content; Mg is one of the main constituents of the refractory materials used in steel manufacture. The nature of the inclusions does not differ between the D1_W, D2_W and D1bis_W alloys. Quantitative data are given in Table 5. The density of inclusions is seven to ten times higher in D1bis_W compared with D1_W or D2_W. The inclusions are randomly distributed in the γ-austenite and δ-ferrite with a significant number of particles located at the interphase boundaries (about 20% of the particles are located at or near the δ/γ interfaces).

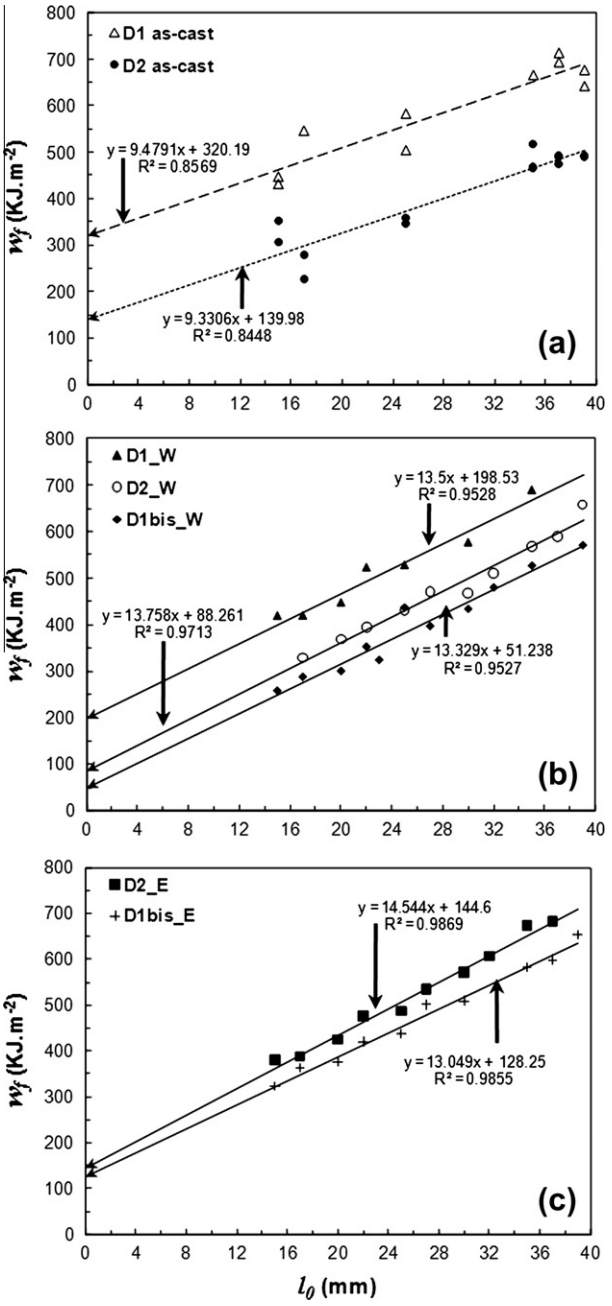

Fig. 5. Variation in the specific work of fracture as a function of the ligament length for separation of the essential work of fracture: (a) D1 and D2 as-cast microstructures; (b) Widmanstätten microstructures D1_W, D1bis_W and D2_W; (c) equiaxed microstructures D1bis_E and D2_E.

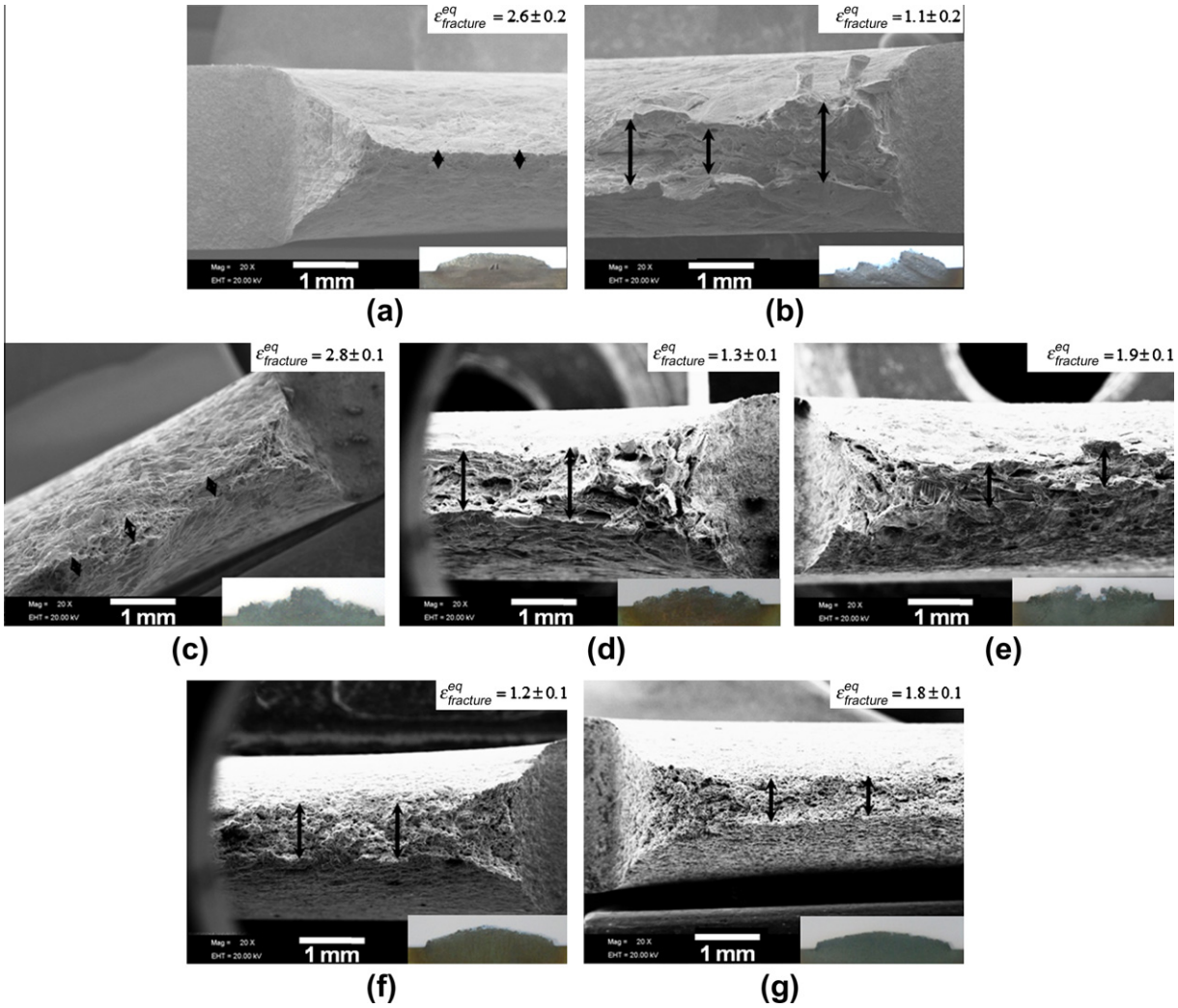

Fig. 6. Fracture micrographs and profiles of the broken DENT specimens: as-cast conditions (a) D1 and (b) D2; Widmanstätten microstructures (c) D1_W, (d) D2_W and (e) D1bis_W; equiaxed microstructures (f) D2_E and (g) D1bis_E.

The results are now analysed with respect to the different microstructures. Three different groups are defined: (i) as-cast microstructures; (ii) Widmanstätten model microstructures; (iii) equiaxed model microstructures. An overview of the results is given in Table 3.

3.1. As-cast microstructures

In the as-cast conditions, the EWF at 1050 °C is equal to ~320 and ~140 kJ m^{-2} for the D1 and D2 alloys, respectively (Table 3). Alloy D1 is thus twice more resistant to ductile tearing than alloy D2. However, the results are strongly dispersed, which places significant uncertainty on the estimation of the EWF (see Fig. 5a). This point will be discussed later in Section 4.1. The fracture profile of grade D1 in the as-cast conditions is predominantly flat along the entire ligament (see Fig. 6a). A classical ductile profile with well-defined dimples is observed at the micro-scale. The crack propagates with a constant thickness reduction, with a steady-state geometry of the FPZ. In contrast, the fracture profile of the D2 in the as-cast conditions is irregular and shows only a few dimples (see Fig. 6b). An estimation of the equivalent strain to fracture for each alloy in the as-cast conditions is provided in Table 3. Several elements must be highlighted when considering Fig. 7a. The strain at the onset of damage nucleation $\varepsilon^{eq}_{damage}$ is very different in the two grades. The density of damage sites starts to increase at $\varepsilon^{eq}_{damage} = 0.5 \pm 0.2$ for alloy D2, whereas it must reach $\varepsilon^{eq}_{damage} = 1.4 \pm 0.2$ in alloy D1. This conforms to the EWF variations. The origin of the difference between D1 and D2 is discussed in Section 4.2.

3.2. Widmanstätten model microstructures

The linear relationships obtained via the EWF method for the model microstructures with a Widmanstätten morphology, i.e. D1_W, D1bis_W and D2_W, are shown in Fig. 5b, with the results summarized in Table 3. D1_W is twice as resistant to tearing as D2_W. This difference is consistent with the measurements on as-cast D1 and D2, although the absolute values are lower, a point which will be discussed in Section 4.1. As shown in Fig. 7a, the void

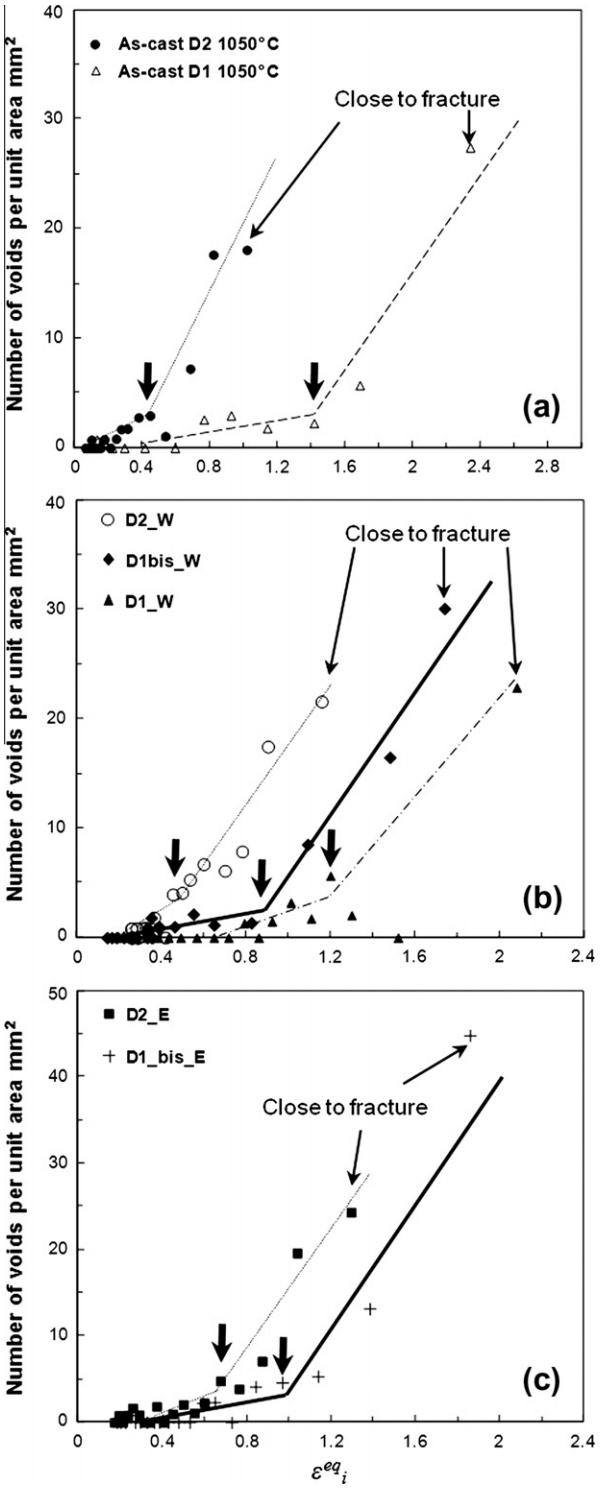

Fig. 7. Evolution of the damage as a function of equivalent strain for each investigated microstructure: (a) D1 and D2 as-cast microstructures; (b) Widmanstätten microstructures D1_W, D1bis_W and D2_W; (c) equiaxed microstructures D1bis_E and D2_E. The arrows emphasize the critical point at which the density of voids increases significantly.

density starts to increase at $\varepsilon^{eq}_{damage} = 0.5 \pm 0.2$ in D2_W, and at $\varepsilon^{eq}_{damage} = 1.2 \pm 0.2$ in D1_W. The origin of the difference between D1_W and D2_W is discussed in Section 4.2. D1bis_W exhibits poor hot tearing resistance (51 kJ m^{-2}) compared with D1_W (199 kJ m^{-2}), although the chemical composition as well as the microstructure are very similar. The strain at the onset of damage nucleation is different, i.e. $\varepsilon^{eq}_{damage} = 0.8 \pm 0.2$ for D1bis_W, and $\varepsilon^{eq}_{damage} = 1.2 \pm 0.2$ for D1_W. The fracture strains scale with $\varepsilon^{eq}_{damage}$ as $\varepsilon^{eq}_{fracture} = 1.9 \pm 0.1$ for D1bis_W and $\varepsilon^{eq}_{fracture} = 2.8 \pm 0.1$ for D1_W (see Table 3).

The difference in inclusion content, much larger in D1bis_W, is an indication of the origin of this difference, discussed in detail in Section 4.3. Typical fracture surfaces of D1_W, D2_W and D1bis_W DENT specimens are shown in Fig. 6c–e. There are no major differences in terms of fracture profiles. These three microstructures exhibit an irregular fracture profile.

3.3. Equiaxed model microstructures

The variations in the total work of fracture as a function of the ligament length are reported in Fig. 5c for the model equiaxed microstructures (see data in Table 3). The linear relationship between w_f and l_0 holds. The EWFs of D2_E and D1bis_E are comparable, with a slightly larger value for the D2_E microstructure (see Table 3). They present a flat profile along the entire ligament (see Fig. 6f and g), but with different $\varepsilon^{eq}_{fracture}$ and $\varepsilon^{eq}_{damage}$ (see Table 3). The difference in fracture resistance of a Widmanstätten γ morphology compared with the equiaxed γ morphology is explained in Section 4.4.

3.4. Fracture micromechanisms

For all DENT specimens the voids are always observed at the δ/γ interphase boundaries, propagating along the interface or within the δ matrix (see an example for D2_W in Fig. 8). No crack was observed in the γ phase. These observations are in good agreement with those carried out along the edge of the hot rolled material. The phenomenon responsible for cracking initiation involves growth and coalescence of voids ahead of a blunted crack tip (see Fig. 9).

4. Discussions

4.1. As-cast vs. model microstructures: influence of microstructure heterogeneities

The application of the EWF concept at high temperature on as-cast microstructures provides clear trends, but the dispersion is important. Metallographic characterizations carried out along the thickness of the as-cast slabs revealed large spatial heterogeneities in the γ phase volume fraction and in the average γ lath thickness (see Table 4). This gradient of microstructure appears in the D2 as well as in the D1 as-cast slabs (see Fig. 10 for an illustration in D2). The microstructure heterogeneity through the slab thickness can be explained by the difference in cooling rate between the skin and the interior of the slab: the faster the

Table 3
Summary of the results obtained for each microstructure investigated.

	T (°C)	w_e (kJ m^{-2})	αw_p (kJ m^{-3})	R^2	$\varepsilon_f^{fracture}$	ε_f^{damage}
D1 as-cast	1050	320 ± 41	9.5 ± 1.4	0.86	2.6 ± 0.2	1.3 ± 0.2
D2 as-cast	1050	140 ± 38	9.3 ± 1.3	0.84	1.1 ± 0.2	0.5 ± 0.2
D1_W	1050	199 ± 33	13.5 ± 1.3	0.95	2.8 ± 0.1	1.2 ± 0.2
D1bis_W	1050	51 ± 26	13.3 ± 0.9	0.95	1.9 ± 0.1	0.8 ± 0.2
D2_W	1050	88 ± 24	13.8 ± 0.8	0.97	1.3 ± 0.1	0.5 ± 0.2
D1bis_E	1050	128 ± 16	13.0 ± 0.6	0.99	1.8 ± 0.1	0.8 ± 0.2
D2_E	1050	145 ± 16	14.5 ± 0.6	0.99	1.2 ± 0.1	0.5 ± 0.2

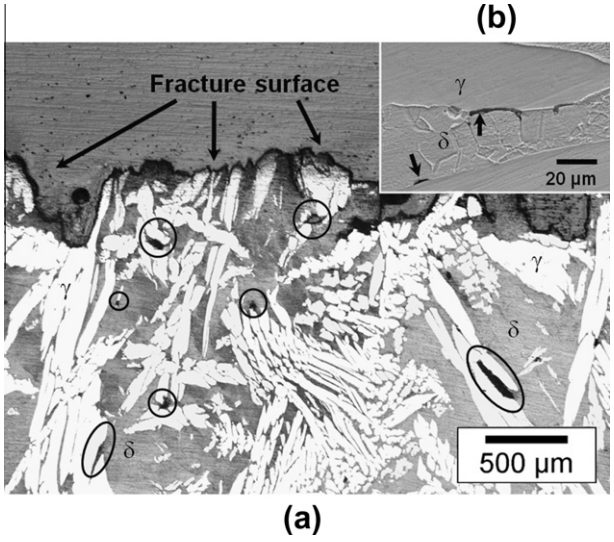

Fig. 8. (a) Optical micrograph and (b) SEM micrograph of a region close to the fracture of a DENT specimen presenting a Widmanstätten microstructure (D2_W); voids nucleate by partial decohesion of the δ/γ-austenite interphase boundary (see the arrows in (b)).

cooling rate, the thinner the γ laths. The microstructural differences between both grades could stem from the chemical composition as well as from the process conditions. The dispersion of the as-cast microstructure characterizations was expected. The as-cast microstructures were too heterogeneous to perform reproducible investigations delivering non-ambiguous conclusions about the parameters playing a role, hence motivating the generation of more homogeneous model microstructures.

The use of homogeneous microstructures improves the quality of the results by reducing the dispersion, as indicated by linear regression coefficients much closer to unity (see Table 3). The main conclusions are similar when comparing the as-cast results with the model Widmanstätten results: (i) D1 is twice as resistant to crack propagation as D2; (ii) the fracture surfaces and profiles, equivalent strain to fracture and damage mechanisms are similar in the as-cast and model microstructures. However, the EWFs (w_e) are much larger in the as-cast microstructures (see Table 3). The heterogeneity of the as-cast microstructures can partly account for these differences by increasing the dispersion and reducing the linear regression coefficient, leading to a lower accuracy of the estimated EWF. In addition, a larger γ lath size in the model microstructures D1_W and D2_W can also be invoked to account for the smaller w_e compared with the as-cast materials. This trend is more significant for alloy D1. For instance, in the model microstructure D1_W the γ laths are twice as thick

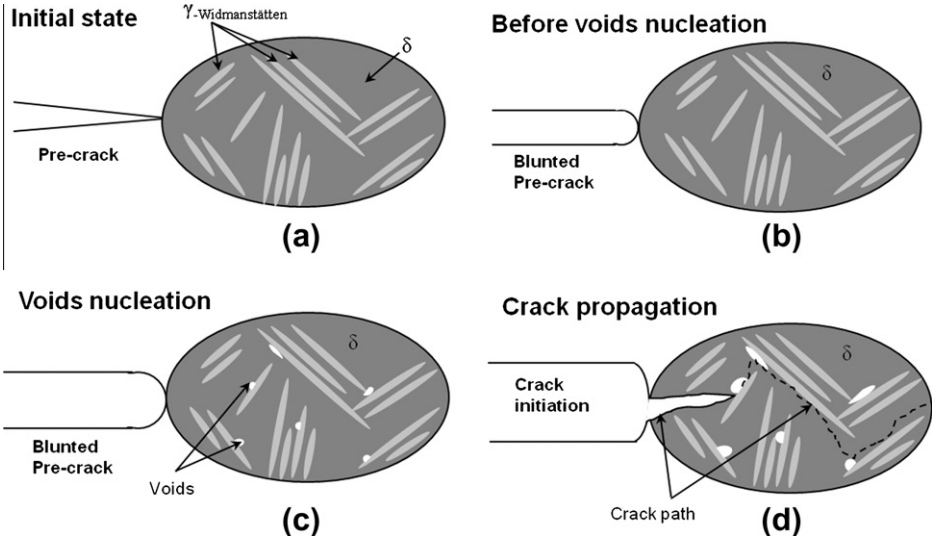

Fig. 9. Schematic illustration of the damage and fracture process taking place in the fracture process zone of duplex stainless steels; (a) initial state; (b) onset of the crack tip blunting; (c) damage nucleation; (d) void coalescence and crack initiation.

Table 4
Comparison between the as-cast microstructures of the alloys D1 and D2.

	D1 as-cast			D2 as-cast		
	e_γ (μm)	γ (%)	δ (%)	e_γ (μm)	γ (%)	δ (%)
Slab skin (2 mm)	7 ± 2	49 ± 1.4	51	20 ± 2	65 ± 3.5	35
Columnar zone (10 mm)	23 ± 2	47 ± 2.3	53	45 ± 3	58 ± 2.4	42
Transition zone (60 mm)	24 ± 2	42 ± 3.1	58	45 ± 4	50 ± 3.2	50
Centre of the slab (100 mm)	21 ± 3	37 ± 3.7	63	38 ± 3	50 ± 2.5	50

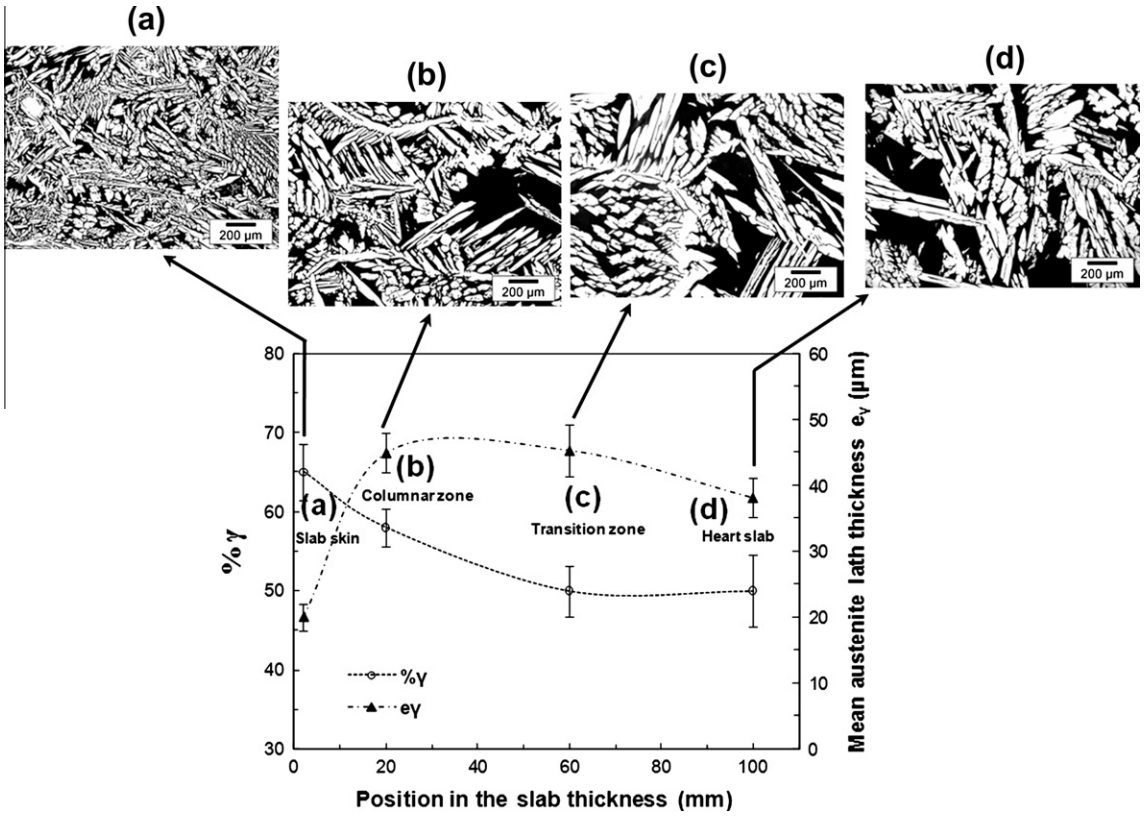

Fig. 10. Illustration of the alloy D2 as-cast slab heterogeneity through thickness: (a) slab skin; (b) columnar zone; (c) transition zone; (d) centre of the slab. The austenite is in white and ferrite in black.

as the columnar zone of the as-cast material, which is the region where the ligament is located. In alloy D2 the γ laths thickness is about 45 μm in the as-cast conditions in the columnar zone, whereas it is about 60 μm in the model microstructure D2_W.

4.2. D1 vs. D2: influence of the phase rheology

According to the experimental results, D1 is twice as resistant to hot cracking as D2, for the as-cast as well as for the model Widmanstätten microstructures. The differences in terms of phase ratio and γ lath size between D1_W and D2_W were significantly reduced thanks to the production of model microstructures with controlled γ content and lath size. Furthermore, it was determined that D1_W and D2_W have very similar inclusion contents (see Table 5). As a result, the key parameter expected to affect the failure behaviour is the mechanical differences between the δ and γ phases. It has been suggested in the literature that the poor hot workability of DSS can be partly explained by strain partitioning between the softer δ phase and the harder γ phase [3,6,13,38]. However, there is a lack of quantitative data about the high temperature micro-scale strain distribution in these alloys.

Table 5
Densities of inclusions determined by both methods in the D1_W and D1bis_W microstructures.

Density of inclusions (no. per mm^2)	D1_W	D1bis_W	D2_W
Manual method			
γ-Austenite	41	477	50
δ-Ferrite	47	504	43
δ/γ Interfaces	23	183	26
Total	111	1165	119
Automatic method			
Total	150	1091	143

A novel development of the classical microgrid technique allowing the measurement of deformation at the microstructure scale in laboratory hot worked steels was recently initiated by Pinna et al. [39] and further developed by Hernandez-Castillo [14] and Martin [40], and applied to both microstructures D1_W and D2_W in order to determine the strain distributions after a 30% reduction by plane strain compression at 850 °C and 1 s^{-1}. The details of the experimental procedures and data reduction scheme are described elsewhere [40]. The strain maps corresponding to steels D1 and D2 are shown in Fig. 11a and b, respectively. Qualitative observations on the deformation pattern can be readily made. First, the strain maps show that the deformation is heterogeneously distributed in both grades; some areas are only slightly deformed whereas others are strongly deformed. Furthermore, the deformation is accommodated more by the δ-ferrite than by the γ-austenite, with the largest strains near the δ/γ interphase boundaries. Shear bands are also observed. Locally the ratio $(\varepsilon^{\delta}_{eq}/\varepsilon^{\gamma}_{eq})$ of the deformation in both phases in the neighbourhood of the interphase boundary fluctuates between 2 and 3, and in a few areas this ratio can reach 5. These results are in agreement with the observations carried out close to the fracture in the DENT specimens showing that voids nucleate by partial decohesion of the δ/γ interphase boundaries (see Fig. 8). The strain distributions look similar for the two grades.

A more quantitative treatment of the strain partitioning can be made by calculating the average deformation of each phase for both microstructures. The strain partitioning is quantified by the ratio between the average deformation in the δ phase divided by the average deformation in γ-austenite $(\bar{\varepsilon}^{\delta}_{eq}/\bar{\varepsilon}^{\gamma}_{eq})$. The results show that in both microstructures δ-ferrite accommodates more deformation compared with γ-austenite, but the strain contrast between the δ and γ phases is significantly larger in D2_W compared with D1_W. In the D1_W microstructure the δ-ferrite deforms on average 30% more than the γ-austenite, whereas in D2_W the δ-ferrite deformed 60% more than the γ-austenite. This difference between D1 and D2 can be attributed to the different chemical compositions, especially the Mo content. The larger mismatch in D2 will induce high growth rates for voids nucleated at the δ/γ interfaces. Indeed, as shown by Li and Guo [41], the rate of growth of voids located at a bimaterial interface is much faster compared with a corresponding homogeneous material, and this effect increases with increasing mismatch. This conclusion was derived based on detailed finite element axisymmetric unit cell calculations with a spherical void at the interface between two elastic–plastic materials. The main reason is that the local stress triaxiality in the soft material is larger than the overall applied triaxiality, leading to faster growth and earlier void coalescence. This is reminiscent of similar ductile failure problems involving soft zones constrained between harder layers [42,43]. Note that a more quantitative determination of the flow properties of the phases using finite element-based inverse identification will be presented elsewhere.

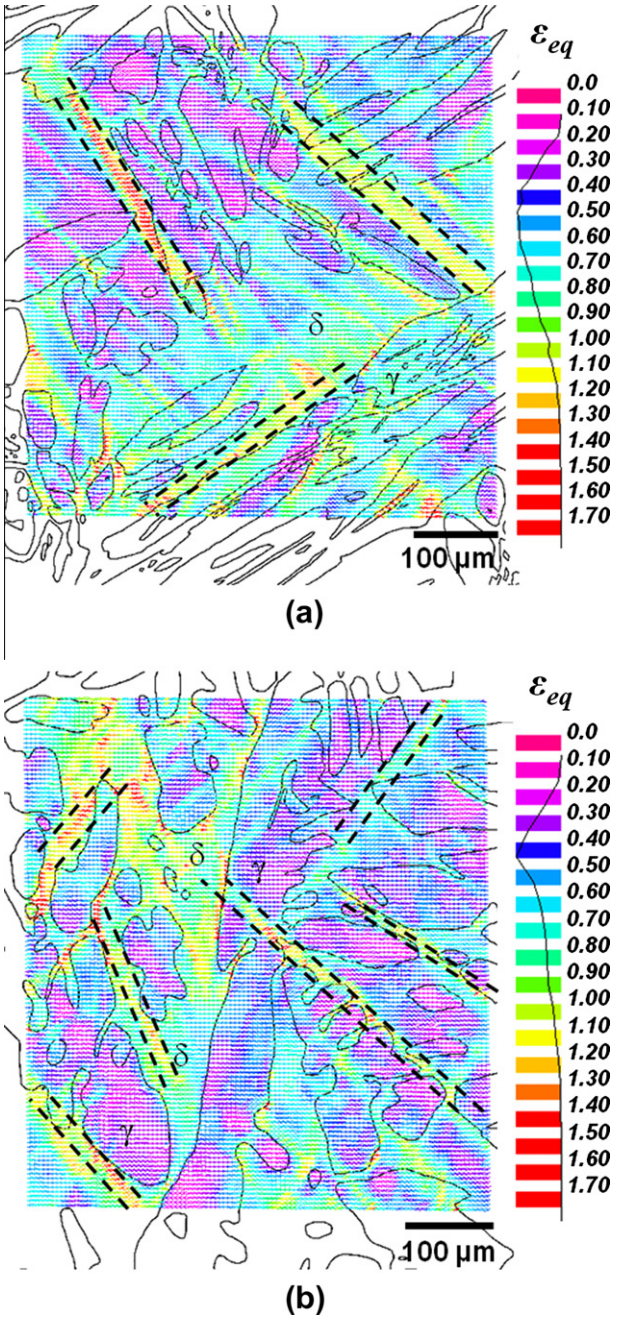

Fig. 11. Equivalent strain maps of the (a) D1_W microstructure and (b) D2_W microstructure. The undeformed microstructures are superimposed on the equivalent strain maps to clearly show where in the microstructure the strains are distributed. The compression axis corresponds to the vertical axis and the dotted lines emphasize the development of shear bands.

4.3. D1 vs. D1bis: influence of the inclusion content

D1 and D1bis are both 2205 conventional duplex steels, with the same chemical composition in terms of major elements (see Table 1). In addition, as both microstructures D1_W and D1bis_W show a Widmanstätten microstructure with a proportion of about 45% γ phase and a similar γ lath size, these parameters cannot be invoked to explain the different hot cracking resistance of D1_W and D1bis_W.

As pointed out in the literature by several authors [2,5], the S content can be very detrimental to the hot workability of duplex steels. Several measurements of the S content were performed for each microstructure. The measured S content was always under 5 p.p.m., whatever the microstructure, D1_W or D1bis_W.

However, significant differences were observed in terms of inclusion content between D1_W and D1bis_W. Fig. 12a and b shows typical micrographs at 500× magnification confirming that the density of inclusions is seven to ten times lower in D1_W compared with D1bis_W. This is the obvious origin of the difference in tearing resistance. Damage characterization carried out on the broken DENT specimens (Fig. 8) demonstrated that the voids always nucleated by decohesion of the δ/γ interfaces and grew within the δ phase. Hence, the lower the inclusion content, the lower the number of potential void nucleation sites at the δ/γ interfaces, and the larger the deformation needed to grow voids until they reach coalescence. Indeed, the relative void spacing is larger [44]. The automatic procedure provides additional information about the sizes of the particles. The average diameters of the inclusions in D1_W and in D1bis_W are very close, about 1.9 μm in the D1_W microstructure and about 1.4 μm in the D1bis_W microstructure. In addition, the size distribution functions exhibit a similar shape (Fig. 12c and d). Most inclusions have a diameter between 1 and 2 μm. Hence, the particle size does not constitute an essential factor distinguishing the tearing resistances of D1_W and D1bis_W.

These results can be discussed and interpreted using a simple mechanical model for the EWF (see Cotterell and Reddel [33]):

$$w_e = k\sigma_c\delta_c \tag{5}$$

where k is a factor depending on the shape of the load–displacement curve, σ_c is a critical stress which can be considered as the mean value of the maximum stress reached in the ligament, and δ_c is a critical displacement which corresponds to the elongation that must be imposed on the representative elementary volume of material at the blunted crack tip (FPZ) leading to complete fracture. This critical displacement can be written as:

$$\delta_c = X_c - X_0, \tag{6}$$

where X_0 and X_c are the initial and final (at fracture) height of the FPZ. It corresponds to the band of material in which, at some point in the deformation history, all the

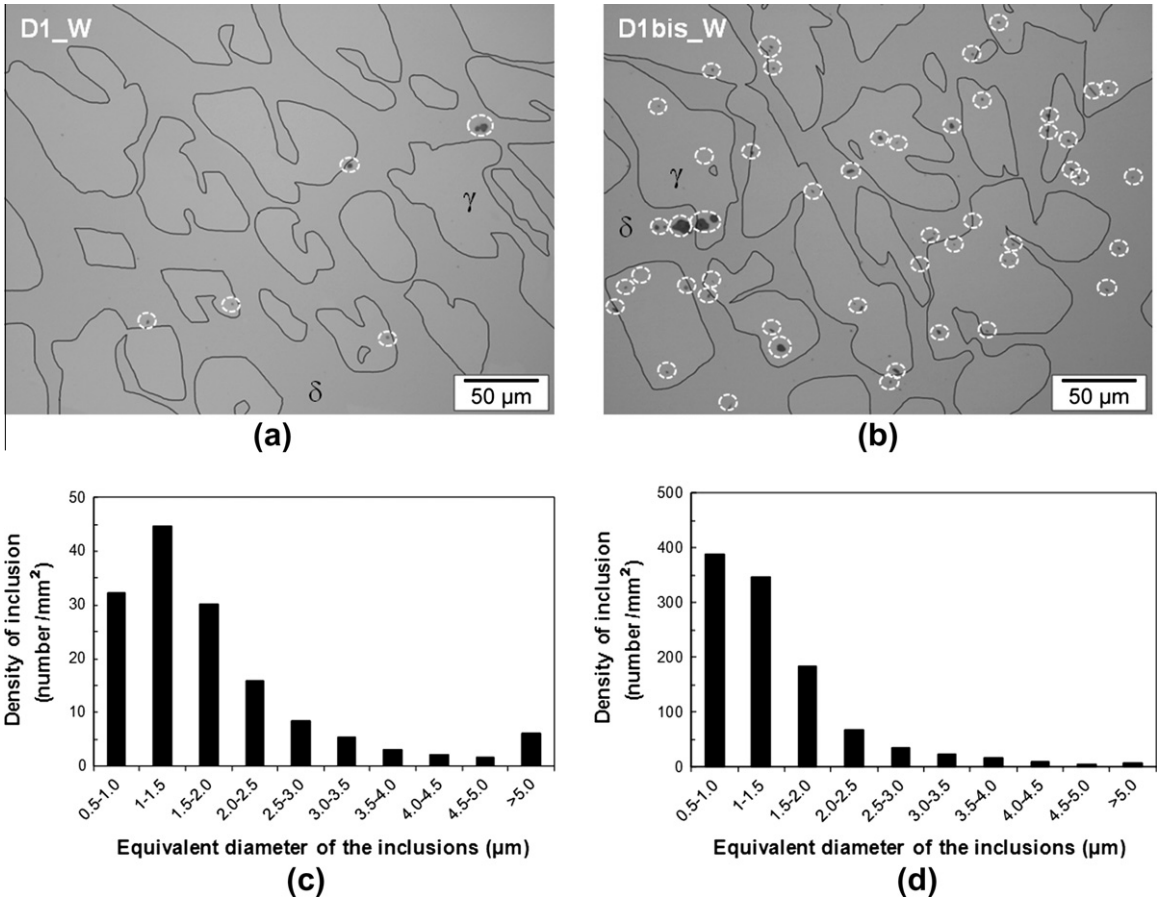

Fig. 12. SEM micrographs to illustrate the difference in terms of inclusion content between (a) D1_W and (b) D1bis_W. The inclusions are circled in white and the interfaces between ferrite and austenite are highlighted to determine the location of the particles. (c and d) The size distribution of the inclusions for (c) D1_W and (d) D1bis_W.

deformation and damage localizes. The corresponding critical strain can be defined as:

$$\varepsilon_c = \ln(X_c/X_0) \tag{7}$$

leading to

$$\delta_c = X_0(\exp(\varepsilon_c) - 1) \tag{8}$$

Applying Eq. (5) to the different microstructures gives, respectively,

$$w_e^{D1\_W} = k\sigma_c^{D1\_W} X_0^{D1\_W}\left(\exp\left(\varepsilon_c^{D1\_W}\right) - 1\right) \tag{9a}$$

$$w_e^{D1bis\_W} = k\sigma_c^{D1bis\_W} X_0^{D1bis\_W}\left(\exp\left(\varepsilon_c^{D1bis\_W}\right) - 1\right) \tag{9b}$$

The microstructures being the same, the characteristic lengths X_0 can be assumed to be equal as well as the stress–strain responses, hence the ratio between $w_e^{D1\_W}$ and $w_e^{D1bis\_W}$ can be written as:

$$\left(w_e^{D1\_W}/w_e^{D1bis\_W}\right) = \left[\exp\left(\varepsilon_c^{D1\_W}\right) - 1\right]/\left[\exp\left(\varepsilon_c^{D1bis\_W}\right) - 1\right] \tag{10}$$

Using the fracture strains indicated in Table 3, the ratio $w_e^{D1\_W}/w_e^{D1bis\_W}$ is equal to ~3, in reasonable agreement with the experimental ratio $w_e^{D1\_W}/w_e^{D1bis\_W} \approx 4$.

4.4. Widmanstätten vs. equiaxed: influence of the phase morphology

The difference in hot tearing resistance between the equiaxed and Widmanstätten morphologies, i.e. between D2_E and D2_W or between D1bis_E and D1bis_W, is more difficult to explain. Note first that the E and W morphologies have similar phase ratios. We may expect that the W morphology constraints the δ phase more than the equiaxed morphology and that this accelerates the ductile damage process. But then why would D2_E and D2_W exhibit similar fracture strains (see Table 3)? The same holds for D1bis_E and D1bis_W. The difference in constraint is thus probably quite moderate, the δ channels being highly constrained in both morphologies. Other possible reasons involve: (i) a difference in phase rheology between the E and W microstructures; (ii) a difference in the nature of the interphase boundaries; (iii) an effect of the morphology on the crack path. These three factors are considered successively.

The two morphologies were generated using different heat treatments. The partitioning of the alloying elements among δ-ferrite and γ-austenite may thus be different depending on the morphology. Such differences can, on the one hand, change the rheology contrast between the two phases due to the strengthening effect of some alloying elements, like N or Mo, and, on the other hand, affect the softening behaviour of the δ and γ phases. However, the partitioning of the alloying elements between the two phases is not significantly different among the two morphologies. The rheology is clearly not the key parameter here.

Pinol-Juez et al. [8] compared, using a high temperature torsion test, the ductility of a standard DSS in the as-cast conditions and after hot rolling. The two microstructures showed different flow curves, and the toughness was reduced in the as-cast condition compared with the hot rolled material. The deformation mechanisms were dissimilar. Pinol-Juez et al. [8] essentially attributed these differences to the nature of the interphase boundaries. In the as-cast conditions the δ/γ interfaces mainly present a Kurdjumov–Sachs orientation relationship, with a semi-coherent character. This coherency of the δ/γ interfaces does not allow accommodation of the deformation by interphase boundary sliding. The authors suggested that the predominant damage mechanism was the nucleation of voids at the δ/γ interfaces and preferential shearing of the ferrite. In contrast, in the microstructure after hot rolling the δ/γ interfaces are incoherent due to the combined effect of strain and softening mechanisms. Sliding at the δ/γ interfaces was the predominant mechanism, allowing better accommodation of the deformation. In the present work we checked that the interphase boundaries involve a Kurdjumov–Sachs orientation relationship in the as-cast as well as in the W microstructures, whereas in the E microstructure δ-ferrite and γ-austenite did not reveal any preferential orientation relationship [45]. Therefore, the nature of the interphase boundaries could contribute to the difference in hot tearing resistance when comparing the two morphologies.

Nevertheless, the difference between E and W can probably be better explained by referring again to the mechanical analysis in Section 4.3. The EWF corresponding to each morphology, E and W, can be written as, respectively:

$$w_e^E = k\sigma_c^E X_0^E\left(\exp(\varepsilon_c^E) - 1\right) \tag{11a}$$

$$w_e^W = k\sigma_c^W X_0^W\left(\exp(\varepsilon_c^W) - 1\right) \tag{11b}$$

In the W microstructures, i.e. D1bis_W and D2_W, the crack is forced to propagate between two austenite laths. The crack path depends on the orientation of the austenite laths (see Fig. 13a). The mean ferrite channel thickness gives $X_0^{D1bis\_W} \approx 40$ μm and $X_0^{D2\_W} \approx 30$ μm, respectively. In the E microstructures, i.e. D1bis_E and D2_E, the characteristic length is the spacing between austenite particles (Fig. 13b): $X_0^{D1bis\_E} \approx 80$ μm and $X_0^{D2\_E} \approx 65$ μm. If we consider that the critical strain is the equivalent strain at fracture, Table 3 indicates that $\varepsilon_c^E \approx \varepsilon_c^W$ for a given alloy. In addition, as the maxima of the load displacement curves are similar, i.e. $\sigma_c^E \approx \sigma_c^W$ for a given alloy, the ratio between the EWF can be estimated as:

$$\begin{aligned}(w_e^E/w_e^W) &= [k\sigma_c^E X_0^E(\exp(\varepsilon_c^E) - 1)]/[k\sigma_c^W X_0^W(\exp(\varepsilon_c^W) - 1)] \\ &\approx X_0^E/X_0^W\end{aligned} \tag{12}$$

where X_0 is a characteristic length as defined in Fig. 13. Using the approximate values of the characteristic lengths, the ratio X_0^E/X_0^W is about 2 for D1bis and D2. This value agrees very well with the experimental ratio w_e^E/w_e^W equal to 1.6 and 2.4 for D2 and D1bis, respectively.

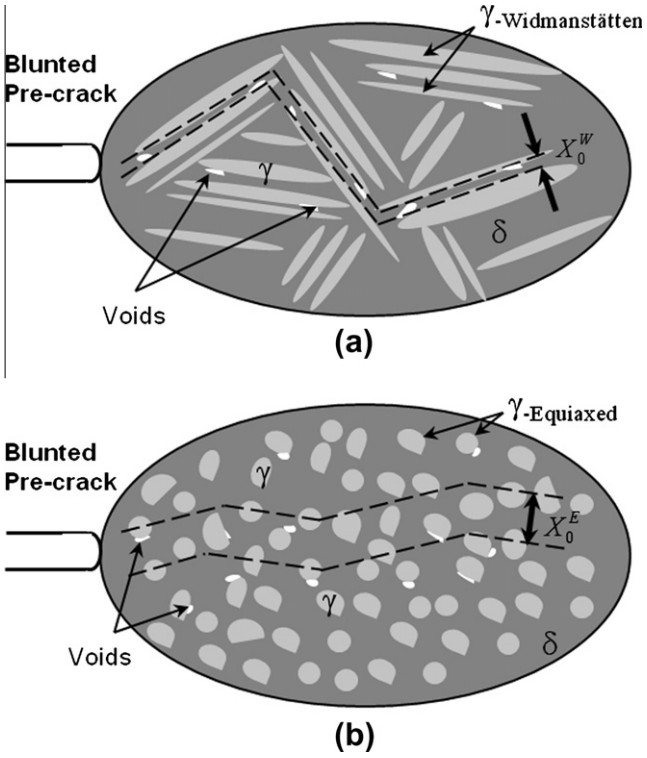

Fig. 13. Schematic definition of the characteristic length X_0 for each morphology of γ-austenite: (a) Widmanstatten morphology W; (b) equiaxed morphology E.

5. Conclusions

The EWF concept has been demonstrated to be a reliable and discriminating tool to quantify the high temperature tearing resistance and to generate a physically relevant fracture indicator. It can be used to guide the optimization of microstructures for successful hot forming operations. The main conclusions emerging from comparisons of the different DSSs and microstructures investigated in this work are as follows.

- In the as-cast condition the Ni- and Mo-rich D1 DSS alloy is twice as resistant to hot tearing as the Mn-rich D2 alloy. The as-cast microstructures exhibit a high degree of heterogeneity leading to significant dispersion in the cracking test results.
- In order to decrease dispersion and to investigate the influence of several microstructural parameters (phase morphology, inclusion content, etc.) model microstructures were produced by proper control of the δ-ferrite → γ-austenite phase transformation with various phase proportions and various sizes and shapes of the microstructural constituents.
- The EWF measured at 1050 °C confirmed that the D1 alloy is twice as resistant to hot tearing as D2, with much less dispersion in the results.
- The strength contrast between the ferrite and the austenite phases varies when comparing high temperature strain maps obtained for the D1 and D2 alloys, which partly explains the difference in hot cracking resistance.
- The inclusion content must be very well controlled, since it is at the origin of the void nucleation process and also affects the onset of void coalescence, which depends on inclusion spacing. Damage was preferentially observed at the δ/γ interfaces, where it nucleates and grows faster than inside homogeneous regions within the phases.
- The austenite morphology has a significant impact on the high temperature fracture resistance, which is twice as great for the equiaxed compared with the Widmanstätten morphology.
- A simple mechanical model for the fracture process zone response is used to predict the relative values of EWF for different microstructures linking the fracture energy to the characteristic microstructure lengths.

Acknowledgements

The authors thank APERAM and the Centre National de la Recherche Scientifique for supporting this work. The support of S.K.Y. by the Wallonia region through the first post-doctoral project CRACKHOT is also acknowledged as well as the support of the Belgian Science Policy through the projects IAP 6/24 and IAP 7/42. L.D. is mandated by the FSR-FNRS (Belgium).

Appendix A

For a linear regression $y = ax + b$, the standard deviation s_a of the slope is given by the relation:

$$s_a = \left[\frac{\sum_{i=1}^{n}(y_i - \hat{y}_i)^2}{(n-2)\sum_{i=1}^{n}(x_i - \bar{x})^2}\right]^{1/2} \quad \text{(A1)}$$

where n is the number of (x_i, y_i) data, $\bar{x}$ is the mean of the x values, and $\hat{y}_i$ are the values of y_i on the regression line at the corresponding value of x_i (i.e. fitted y_i values). The standard deviation s_b of the intercept for $x = 0$ is calculated from least squares principles as:

$$s_b = \left[\frac{\sum_{i=1}^{n}(y_i - \hat{y}_i)^2 \sum_{i=1}^{n} x_i^2}{n(n-2)\sum_{i=1}^{n}(x_i - \bar{x})^2}\right]^{1/2} \quad \text{(A2)}$$

References

[1] Charles J. Steel Res Int 2008;79:455.
[2] Liou HY, Pan YT, Hsieh RL, Tsai WT. J Mater Eng Perform 2001;10:231.
[3] Duprez L, De Cooman BC, Akdut N. Z Metall 2002;93:236.
[4] Iza-Mendia A, Gutierrez I. In: Proceedings of the duplex 2007 international conference and expo, Grado, Italy; 2007 (CD).
[5] Tsuge S. In: Proceedings of the International conference on stainless steels, Chiba, Japan; 1991. p. 799–806.
[6] Iza-Mendia A, Pinol-Juez A, Urcola JJ, Gutierrez I. Metall Mater Trans A 1998;29:2975.

[7] Pinol-Juez A, Iza-Mendia A, Gutierrez I, Urcola JJ. Key Eng Mater 1997;127–131:1025.
[8] Pinol-Juez A, Iza-Mendia A, Gutierrez I. Metall Mater Trans A 2000;31:1671.
[9] Dehghan-Manshadi A, Barnett MR, Hodgson PD. Mater Sci Technol 2007;23:1478.
[10] Dehghan-Manshadi A, Hodgson PD. J Mater Sci 2008;43:6272.
[11] Cizek P, Wynne BP. Mater Sci Eng A 1997;230:88.
[12] Cizek P, Wynne BP, Rainforth WM. J Microsc Oxf 2006;222:85.
[13] Evangelista E, McQueen HJ, Niewczas M, Cabibbo M. Can Metall Q 2004;43:339.
[14] Hernandez-Castillo LE, Beynon JH, Pinna C, van der Zwaag S. Steel Res Int 2005;76:137.
[15] Cotterell B, Atkins AG. Int J Fract 1996;81:357.
[16] Chehab B, Brechet Y, Glez JC, Jacques PJ, Mithieux JD, Veron M, et al. Scripta Mater 2006;55:999.
[17] Knockaert R, Doghri I, Marchal Y, Pardoen T, Delannay F. Int J Fract 1996;81:383.
[18] Pardoen T, Marchal Y, Delannay F. Eng Fract Mech 2002;69:617.
[19] Pardoen T, Hachez F, Marchioni B, Blyth PH, Atkins AG. J Mech Phys Solids 2004;52:423.
[20] Marchal Y, Delannay F. Int J Fract 1996;80:295.
[21] Mai YW, Pilko KM. J Mater Sci 1979;14:386.
[22] Pardoen T, Marchal Y, Delannay F. J Mech Phys Solids 1999;47:2093.
[23] Marchal Y, Oldenhove B, Daoust D, Legras R, Delannay F. Polym Eng Sci 1998;38:2063.
[24] Mai YW, Cotterell B. Int J Fract 1986;32:105.
[25] Mai YW, Powell P. J Polym Sci 1991;29:785.
[26] Garnier G, Chehab B, Yrieix B, Brechet Y, Flandin L. J Mater Sci 2009;44:5537.
[27] Arkhireyeva A, Hashemi S. Eng Fract Mech 2004;71:789.
[28] Hashemi S, Arkhireyeva A. J Macromol Sci – Phys 2002;B41:863.
[29] Menezes JWA, Abreu H, Kundu S, Bhadeshia H, Kelly PM. Sci Technol Weld Join 2009;14:4.
[30] Monlevade EF, Falleiros IGS. Metall Mater Trans A 2006;37A:939.
[31] Bugat S, Besson J, Gourgues AF, N'Guyen F, Pineau A. Mater Sci Eng A 2001;317:32.
[32] ADCIS. Aphelion V. 3.2. Saint-Contest, France. ADCIS S.A.; 2003.
[33] Cotterell B, Reddel JK. Int J Fract 1977;13:267.
[34] Broberg KB. J Mech Phys Solids 1975;23:215.
[35] Cotterell B, Pardoen T, Atkins AG. Eng Fract Mech 2005;72:827.
[36] Hill R. J Mech Phys Solids 1952;1:19.
[37] Oxford Instruments. INCAFeature. Oxford Instruments Analytical; 2010.
[38] Spigarelli S, El Mehtedi M, Ricci P, Mapelli C. Mater Sci Eng A 2011;528:6919.
[39] Pinna C, Beynon JH, Sellars CM, Bornert M. In: Martin P, MacEwen S, Verreman Y, Lui W, Goldak J, editors. Proceedings of the conference on mathematical modelling in metal processing and manufacturing, Ottawa, Canada; 2000 (CD).
[40] Martin G, Caldemaison D, Bornert M, Pinna C, Bréchet Y, Véron M, et al. Exp Mech, accepted for publication.
[41] Li Z, Guo W. Int J Plast 2002;18:249.
[42] Pardoen T, Brechet Y. Philos Mag 2004;84:269.
[43] Pardoen T, Dumont D, Deschamps A, Brechet Y. J Mech Phys Solids 2003;51:637.
[44] Pardoen T, Scheyvaerts F, Simar A, Tekoglu C, Onck PR. CR Phys 2010;11:326.
[45] Martin G. PhD thesis, Université de Grenoble, France, 2011.